

Structural and magnetic properties of molecular beam epitaxy grown chromium selenide thin films

Anupam Roy ^{1,*}, Rik Dey,¹ Tanmoy Pramanik ¹, Amritesh Rai,¹ Ryan Schalip ¹, Sarmita Majumder ¹,
Samaresh Guchhait ² and Sanjay K. Banerjee¹¹Microelectronics Research Center, The University of Texas at Austin, Austin, Texas 78758, USA²Department of Physics and Astronomy, Howard University, Washington, DC 20059, USA

(Received 23 October 2019; revised manuscript received 30 December 2019; accepted 14 January 2020; published 10 February 2020)

Chromium selenide thin films were grown epitaxially on Al₂O₃(0001) and Si(111)-(7 × 7) substrates using molecular beam epitaxy. Sharp streaks in reflection high-energy electron diffraction and triangular structures in scanning tunneling microscopy indicate flat smooth film growth along the *c* axis, which is very similar to that from a hexagonal surface. The x-ray diffraction pattern confirms the growth along the *c* axis with a *c*-axis lattice constant of 17.39 Å. The grown film is semiconducting, having a small band gap of about 0.034 eV, as calculated from the temperature-dependent resistivity. The antiferromagnetic nature of the film with a Néel temperature of about 40 K is estimated from the magnetic exchange bias measurements. A larger out-of-plane exchange bias, along with a smaller in-plane exchange bias is observed below 40 K. Exchange bias training effects are analyzed based on different models and are observed to be following a modified power-law decay behavior.

DOI: [10.1103/PhysRevMaterials.4.025001](https://doi.org/10.1103/PhysRevMaterials.4.025001)

I. INTRODUCTION

Binary chromium-based chalcogenides exhibit various interesting physical properties with a wide variation in electrical and magnetic properties. A small change in composition changes the physical properties and makes them more fascinating as a material system to study. Wontcheu *et al.* have shown the effect of anion substitution on the structural and magnetic properties of chromium chalcogenides [1]. The chromium selenium system is a large family of compounds with large varieties of stable stoichiometries [e.g., Cr_{1-x}Se, Cr₂Se₃, Cr₃Se₄, Cr₅Se₈, Cr₇Se₈, etc.]. All of these compounds have NiAs-type crystal structure. Due to incomplete *d* orbitals of the transition metal, these NiAs-type structures show interesting magnetic and electrical properties [2]. Different compounds of chromium selenides differ on the Cr vacancies that occur in every second metal layer. Thus, every alternate layer of metal-deficient and metal-rich layers stacks along the *c* axis [3–7]. Magnetic properties of bulk Cr₂Se₃ have been studied extensively before, and it has been shown to be an antiferromagnet below the Néel temperature, *T_N* ~ 43 K. Also, an order-order transition occurs at ~38 K between the low-temperature and high-temperature antiferromagnetic Cr₂Se₃ structures, as observed from neutron diffraction studies [6–9]. Because of Cr vacancies in alternate layers, the moments associated with Cr atoms located on two different layers are different due to different neighboring environments and this leads to the complexity in the magnetic structure below *T_N*.

Previously, chromium selenide systems have been studied to investigate their suitability as a thermoelectric material for intermediate-temperature applications [10–14], intermediate-temperature power generation [13], electrochemical sensors [15], etc. Several groups have studied the structural, magnetic,

electrical, and thermoelectric properties of single-crystal Cr_{2+x}Se_{3-x} compounds grown using the solid-state reaction method [10–13,16], soft chemical and hydrothermal synthesis [15,17,18], and chemical vapor transport method [4,14,19–21]. However, the studies focus mostly on the improvement in thermoelectric properties of transition-metal-doped bulk samples of Cr₂Se₃. The epitaxial growth and different physical properties of Cr₂Se₃ thin films are yet to be explored in detail. Molecular beam epitaxy (MBE) is a highly specialized technique used to grow ultrahigh-purity large-area epitaxial thin films with abrupt interfaces and with precise control over their thicknesses. Compared to other growth techniques, MBE offers greater control to incorporate dopants in thin films. This makes it an even more suitable growth method, as the electrical, magnetic, and thermoelectric properties of this material system can be largely varied with addition of transition-metal/chalcogen dopants [1,9–13,21,22].

In this work, we report the epitaxial growth of Cr₂Se₃ thin films under ultrahigh vacuum (UHV) directly on Al₂O₃(0001) and Si(111)-(7 × 7) surfaces using MBE. Interestingly, we show that the growth occurs along the (001) direction (*c* axis). We present the details of growth, structural, electrical, and magnetic properties characterized by several *in situ* and *ex situ* techniques, e.g., reflection high-energy electron diffraction (RHEED), x-ray diffraction (XRD), scanning tunneling microscopy (STM), x-ray photoelectron spectroscopy (XPS), magnetotransport measurements, etc. We report the exchange bias training behavior of the epitaxial Cr₂Se₃ thin film coupled with a ferromagnet, characterized using magnetoresistance (MR) measurements, and analyzed in detail using different models.

II. EXPERIMENTAL METHOD

Growth. Cr₂Se₃ films were grown in a custom-built MBE growth system (Omicron, Germany) under ultrahigh-vacuum

*anupam@austin.utexas.edu

(UHV) conditions (base pressure $\sim 1 \times 10^{-10}$ mbar). Details of the system have been described elsewhere [23]. A reflection high-energy electron diffraction (RHEED) setup is attached to the MBE system for *in situ* monitoring of surface reconstruction and growth. Substrates used in the experiment were insulating *c*-axis $\text{Al}_2\text{O}_3(0001)$ and P-doped *n*-type $\text{Si}(111)$ wafers (oriented within $\pm 0.5^\circ$) with a resistivity of 1–20 Ω cm. After the substrates were precleaned in acetone and isopropanol, the substrates were introduced into the UHV chamber. Atomically clean, reconstructed $\text{Si}(111)-(7 \times 7)$ surfaces were prepared by the usual heating and flashing procedure [24]. Single-crystal *c*- $\text{Al}_2\text{O}_3(0001)$ substrates were prepared by resistive heating at 600 $^\circ\text{C}$ for 3 h followed by 700 $^\circ\text{C}$ for 30 min. Clean substrate surfaces were examined by *in situ* RHEED. Chromium and selenium fluxes generated by *e*-beam evaporator and effusion cell, respectively, were codeposited on the substrates at an elevated substrate temperature of about 340 $^\circ\text{C}$. The chamber pressure during growth never exceeded 1×10^{-9} mbar and the Se_2/Cr BEP (beam equivalent pressure) flux ratio was kept at about 15. Several samples with thicknesses varying from 5 to 25 nm were grown and the typical growth rate of Cr_2Se_3 films was about 0.1 nm/min.

Characterization. Postgrowth investigations of the samples were carried out by *in situ* RHEED operated at 13 kV, scanning tunneling microscopy (STM) at room temperature (RT) in the constant current mode, and x-ray photoelectron spectroscopy (XPS) with a monochromatic Al $K\alpha$ source ($h\nu = 1486.7$ eV) operating at 15 kV. A Philips X-Pert x-ray diffraction (XRD) system equipped with a Cu x-ray filament source and a PW-3011/20 proportional detector was used for the *ex situ* XRD measurements.

Electrical and magnetic measurements. Transport measurements were carried out with a 9-T Quantum Design physical property measurement system (PPMS) combined with vibrating sample magnetometry (VSM) capable of cooling samples down to ~ 2 K. The measurements were conducted using the standard van der Pauw method with indium dot contacts at the four corners of the large-area rectangular samples.

III. RESULTS AND DISCUSSIONS

A. Growth and characterizations

Bulk crystal growth of Cr_2Se_3 has been achieved previously by various methods, e.g., the ceramic method [6–9], solid-state reaction method [10–13,16], soft chemical and hydrothermal synthesis [15,17,18], and chemical vapor transport method [4,14,19–21]. Using MBE, here we have studied the growth of Cr_2Se_3 thin films of different thicknesses directly on UHV-cleaned $\text{Al}_2\text{O}_3(0001)$ and $\text{Si}(111)-(7 \times 7)$ substrates without any buffer layer.

Figures 1 and 2 display the RHEED patterns observed for the epitaxial Cr_2Se_3 thin film on $\text{Al}_2\text{O}_3(0001)$ and $\text{Si}(111)-(7 \times 7)$ substrates. Insulating crystalline sapphire substrates were chosen due to their hexagonal surface symmetry and to enable electrical measurements of the as-grown films. Figure 1 shows the RHEED images of the substrate before and after growth. Figures 1(a) and 1(b) show the RHEED patterns from the clean $\text{Al}_2\text{O}_3(0001)$ substrate along the

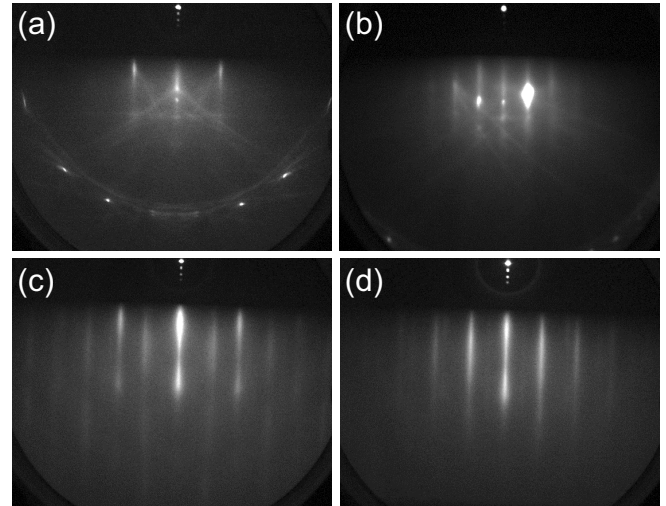


FIG. 1. RHEED images following Cr_2Se_3 growth on $\text{Al}_2\text{O}_3(0001)$ surfaces. (a), (b) RHEED patterns from a clean $\text{Al}_2\text{O}_3(0001)$ surface with the incident electron beam along $[1\ 0\ -1\ 0]$ and $[1\ 1\ -2\ 0]$ orientations of Al_2O_3 , respectively. (c), (d) Corresponding RHEED patterns from the same surface following 15 nm of Cr_2Se_3 growth.

$[1\ 0\ -1\ 0]_{\text{Al}_2\text{O}_3}$ and $[1\ 1\ -2\ 0]_{\text{Al}_2\text{O}_3}$ directions, respectively, after a preheat treatment. Kikuchi lines are clearly observed in the RHEED patterns in Figs. 1(a) and 1(b) indicating a clean and smooth morphology of the substrate. Corresponding RHEED patterns observed after the growth are shown in Figs. 1(c) and 1(d). RHEED patterns from the sapphire substrate disappear completely within a few minutes of the growth at elevated temperature and result in sharp streaky RHEED patterns. In addition, half-order reconstructions are observed in the RHEED patterns reflecting a high crystal

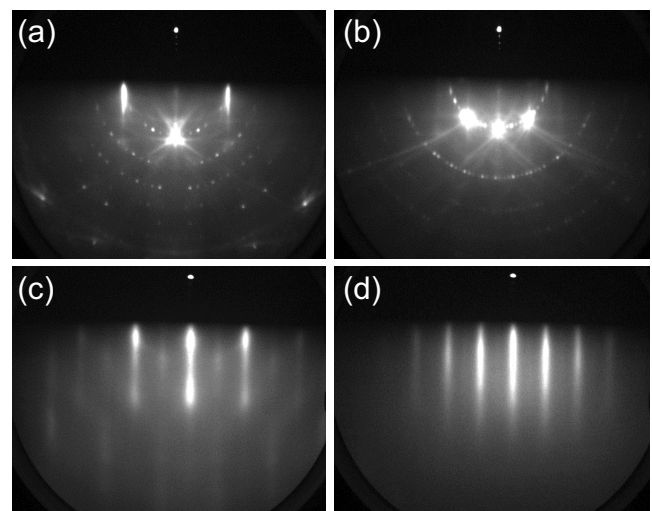


FIG. 2. RHEED images following Cr_2Se_3 growth on $\text{Si}(111)-(7 \times 7)$ surfaces. (a), (b) RHEED patterns from a clean (7×7) surface reconstruction from $\text{Si}(111)$ substrate along $[1\ 1\ -2]$ and $[1\ -1\ 0]$ orientations of Si , respectively. (c), (d) Corresponding RHEED patterns from the same surface following 25 nm of Cr_2Se_3 growth.

quality of the grown film. Streaky RHEED patterns are maintained throughout the growth process following the substrate surface crystal symmetry and the RHEED features are sensitive to both sample and beam orientation.

Similar growth has been achieved on Si(111) substrates, as shown in Fig. 2. RHEED patterns from a reconstructed Si(111)-(7 × 7) surface are shown in Fig. 2(a) for the electron beam along the $[1\bar{1}-2]_{\text{Si}}$ direction and in Fig. 2(b) for $[1\bar{1}0]_{\text{Si}}$ incidence. Corresponding RHEED patterns, following epitaxial growth of Cr_2Se_3 films, are shown in Figs. 2(c) and 2(d). Sharp streaky patterns in RHEED, for the growth on both $\text{Al}_2\text{O}_3(0001)$ and Si(111)-(7 × 7) substrates, suggest well-structured film growth with high crystalline quality and smooth surface morphologies. Several samples with different thicknesses prepared on both substrates show similar RHEED patterns, and for all of them, the RHEED patterns were maintained throughout the entire growth process (as also shown in Fig. S1 in the Supplemental Material [25]; also see Refs. [26–48]). Similar to the growth on $\text{Al}_2\text{O}_3(0001)$ substrates, half-order reconstruction lines are present in the RHEED patterns [Figs. 2(c) and 2(d)]. Furthermore, the growth occurs along the c axis [along the (001) direction], as expected for the growth of a hexagonal thin film on an hcp(0001) or fcc(111) substrate. Similar (001)-oriented hexagonal thin-film growth on fcc(111) surfaces also has been reported for $\text{Cr}_2\text{Te}_3(0001)$, $\text{Bi}_2\text{Te}_3(0001)$, and $\text{Bi}_2\text{Se}_3(0001)$ on Si(111) substrates [23,49,50].

XRD is used to evaluate the structure of the films and to confirm their epitaxial nature. Figure 3(a) shows the XRD patterns from Cr_2Se_3 thin films of different thicknesses grown on $\text{Al}_2\text{O}_3(0001)$ substrates and shows characteristic peaks that correspond to diffraction from the (00 l) family of planes of the Cr_2Se_3 film. The sharp peak at $2\theta = 41.7^\circ$ corresponds to reflection from the (006) plane of the $\text{Al}_2\text{O}_3(0001)$ substrate. The XRD pattern agrees very well with the NiAs-type crystal of Cr_2Se_3 with hexagonal structure [ICSD Collection Code 42705, space group $R\bar{3}$ (148)]. The crystal structure of rhombohedral Cr_2Se_3 is shown in Fig. 3(b). XRD peaks corresponding to the planes (0 0 6) and (0 0 12) of Cr_2Se_3 are indexed in Fig. 3(a). The absence of peaks other than the (00 l) family confirms the epitaxial growth along the c axis of the sapphire substrates. The XRD pattern also rules out any significant presence of any impurities and other known phases of chromium selenide. The extracted c -axis lattice constant of the Cr_2Se_3 film is 17.39 Å, almost invariable for different samples (within 0.2%) and matches closely with the bulk crystal value of 17.38 Å [4].

Figures 3(c) and 3(d) show *in situ* STM studies of the surface of Cr_2Se_3 thin films grown on Si(111)-(7 × 7) surfaces. The structures are characteristically triangular shaped, reflecting the hexagonal crystal structure along the (001) direction. Because of the threefold crystal symmetry of the Si(111) substrate, formation of equilateral triangles is natural. Both hcp(0001) and fcc(111) surfaces have a similar hexagonal Bravais lattice and they differ only in the registry of the third layer [51]. Compared to previous studies of bulk crystals grown via the solid-state reaction method [11,12], we notice diminished sizes of the structures in a thin film (~20–40 nm). Insets show the close-up shape of triangular structures. Closer examination of the triangular domain reveals that the shapes

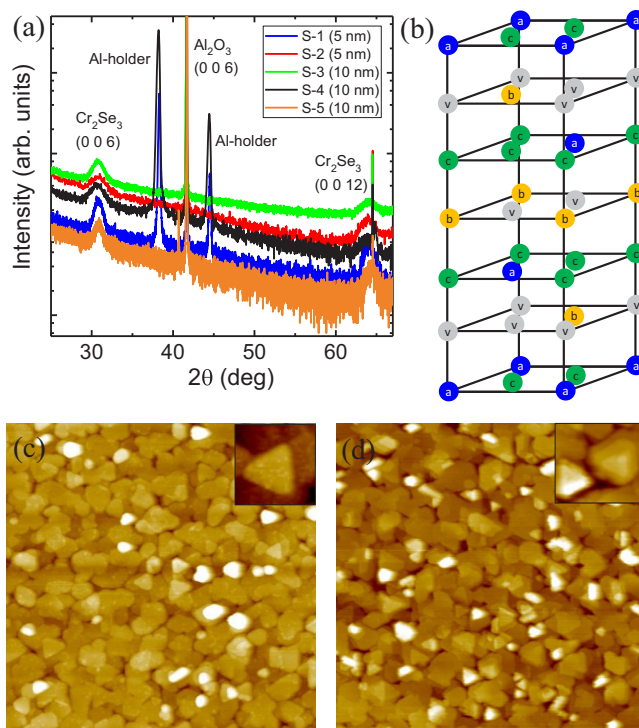


FIG. 3. (a) XRD patterns from single-crystal Cr_2Se_3 thin films of different thicknesses. The pattern shows that the growth is along the (001) direction. (b) Rhombohedral crystal structure for Cr_2Se_3 where Se atoms are abbreviated for simplicity. Cr atoms are shown at three different Wyckoff sites (“a,” “b,” “c”), and vacancy sites are shown as “v” (gray). (c), (d) *In situ* STM studies of 5-nm epitaxial Cr_2Se_3 thin films grown on Si(111)-(7 × 7) surfaces. Several triangular features observed are reflecting the influence of substrate crystal symmetry. (Scan area: $300 \times 300 \text{ nm}^2$; bias voltage: -2.5 V ; tunneling current: 0.7 nA). Insets ($25 \times 25 \text{ nm}^2$) show (c) one such triangular domain and (d) triangular domains stacked up as multiple layers.

are truncated triangular or triangular hexagon. For hexagonal crystal structures, this happens when there is a mismatch in the rate of advancement of adatoms between the two edges during growth [52,53]. The inset of Fig. 3(d) illustrates that multiple triangular domains stack up on top of each other. A similar observation of truncated triangular structures has also been made in the case of hexagonal Cr_2Te_3 thin films grown epitaxially on Si(111)-(7 × 7) surfaces [49].

The elemental compositions of the grown films were examined by *in situ* XPS. Figure 4(a) shows the XPS survey scans of the Cr_2Se_3 thin films. All the major peaks have been identified and assigned to Cr and Se. XPS also confirms the film to be free from the presence of any other elements as impurities. High-resolution XPS analysis of the sample finds peaks at Cr-2 p and Se-3 d edges, as shown in Figs. 4(b) and 4(c), respectively. The Cr-2 p spectrum was fitted using an asymmetric peak shape due to Cr_2Se_3 being a narrow band gap semiconductor. The CASAXPS function LA(1.4,2,2), taken from a previous study on conductive Zn and its oxides, provided an excellent match [54,55]. The binding energies corresponding to the Cr-2 $p_{3/2}$ and Cr-2 $p_{1/2}$ peaks are at 574.4 and 583.8 eV, respectively, giving a doublet splitting of 9.4 eV. Binding energy corresponding to the Cr-3 s peak at 74.3 eV

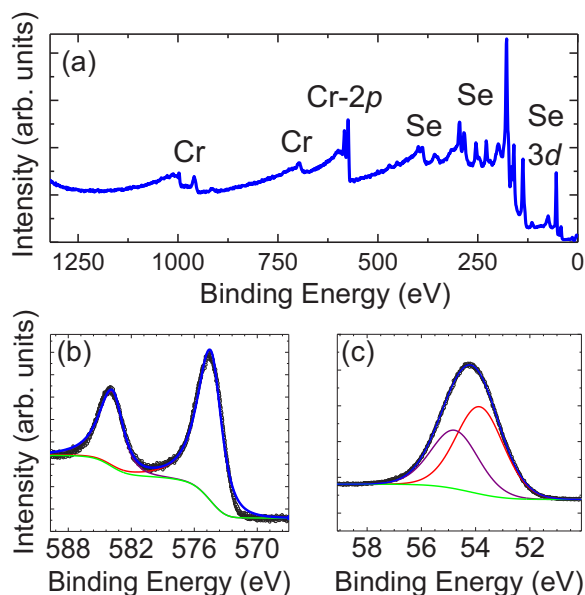


FIG. 4. *In situ* high-resolution XPS spectra of Cr_2Se_3 thin films. (a) Survey scan from Cr_2Se_3 film. (b), (c) are Cr-2*p* and Se-3*d* core-level photoemission spectra from 25 nm of Cr_2Se_3 thin film, respectively, showing chemical shifts corresponding to homogeneous phases of hexagonal Cr_2Se_3 . A Se/Cr ratio of about 1.5 is extracted from the area fit (solid lines) to the experimental data (○).

also matches very well. The positions of the Cr peaks are found to be in good agreement with previous literature values for Cr_2Se_3 [56]. Similarly, the Se-3*d* spectrum is also well fitted using GL(30) peak shapes and its peak location (54.2 eV) matches very well with previous reports [56]. Using the integrated areas under the peaks, a Se/Cr ratio of about 1.5 is obtained.

B. Electrical properties

The 3*d* transition metal chalcogenides show various intriguing electrical and magnetic properties. Different combinations of transition metal and chalcogen atoms can lead to various distinct and complex electrical and magnetic characteristics. For example, $\text{Cr}_{1-\delta}\text{Se}$ are mostly antiferromagnetic and semiconducting for $0 \leq \delta \leq 0.33$, whereas $\text{Cr}_{1-\delta}\text{Te}$ are all ferromagnetic with metallic conductivities for $0 \leq \delta \leq 0.37$. Cr_2Se_3 bulk samples were reported to be narrow band gap semiconductors [1,3,9–11,13,14,19–22,57–59]. The large-area continuous nature of the films and the insulating sapphire substrate enabled us to perform temperature-dependent resistivity measurements of the as-grown films using a standard van der Pauw geometry. Figure 5 shows the electrical properties of a 5-nm epitaxial Cr_2Se_3 thin film grown on an $\text{Al}_2\text{O}_3(0001)$ substrate. Electrical resistivity measured for the temperature range from RT to 77 K, shown in Fig. 5(a), shows semiconducting behavior, i.e., resistance increases with decreasing temperature.

The variation of conductivity (σ) with inverse temperature is shown in Fig. 5(b) on a semilog scale. The low band gap of Cr_2Se_3 may indicate an intrinsiclike behavior of the material at the measured temperature range [14,60]. The con-

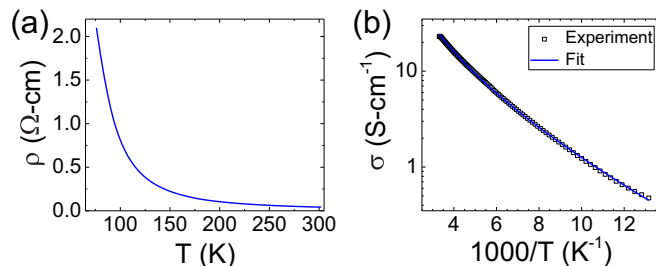


FIG. 5. Electrical transport properties of the 5-nm epitaxial Cr_2Se_3 film grown on $\text{Al}_2\text{O}_3(0001)$ substrate surface. (a) Temperature dependence of electrical resistivity shows an insulating trend. (b) The variation of conductivity is plotted on a semilog scale vs $1/T$.

ductivity of an intrinsic semiconducting material is given by $\sigma = en_i(\mu_e + \mu_h)$, where μ_e and μ_h are carrier mobilities for electrons and holes, respectively; e is the electron charge; and n_i is the intrinsic carrier concentration with $n_i \approx n_0 T^{\frac{3}{2}} e^{-\frac{E_g}{2k_B T}}$. The factor $T^{\frac{3}{2}}$ is due to the variation of effective density of states with temperature and $e^{-\frac{E_g}{2k_B T}}$ is the Boltzmann weight. For an estimation of the band gap, the conductivity is fitted with [60]

$$\log \sigma = C + \frac{3}{2} \log T - \frac{E_g}{2k_B T}, \quad (1)$$

where E_g is the band gap, k_B is the Boltzmann constant, and C is a constant. In Eq. (1), the carrier mobilities are assumed to be constant with temperature. The value of E_g estimated from the fit is about 0.034 eV. [Assuming temperature dependence of the net mobility $(\mu_e + \mu_h) \propto T^p$ and fitting the data with $\log \sigma = C + (\frac{3}{2} + p) \log T - \frac{E_g}{2k_B T}$ in a three-parameter fit instead of the two-parameter fit of Eq. (1), we obtain $p \approx -0.12$ and $E_g \approx 0.037$ eV (see Sec. S2 in the Supplemental Material [25].)] In the literature, it was shown that Si and Ge show intrinsiclike behavior above a temperature T_m , where $k_B T_m$ are about $0.04E_g$ and $0.08E_g$, respectively [60]. The estimated low band gap of Cr_2Se_3 is about $5k_B T$ at 77 K (i.e., $k_B T$ is about $0.2E_g$) indicating that for the entire temperature range (from RT to 77 K) the material may behave intrinsically, and provides a self-consistent check that Eq. (1) is valid to describe the temperature-dependent resistivity.

C. Magnetic properties

Previous studies of Cr_2Se_3 bulk crystals report an antiferromagnetic nature with the Néel temperature (T_N) around 42–45 K [6–9]. It is to be noted that molecular oxygen trapped in the measurement chamber also undergoes an antiferromagnetic transition at about 43 K and can show a similar signature in the magnetic measurement at the same temperature range as in Cr_2Se_3 [61]. To avoid any possible errors due to trapped oxygen, we have adopted a different approach to investigate the magnetic properties of epitaxial Cr_2Se_3 thin films. An 8-nm-thin layer of ferromagnetic Fe is deposited on top of an epitaxial Cr_2Se_3 layer and capped with a 10-nm Ta layer. A schematic of this exchange-biased structure is shown in Fig. S3(a) in Ref. [25]. MR of the stack is studied to examine the exchange bias phenomenon of this antiferromagnetic-

ferromagnetic (AFM-FM) system. The exchange bias effect in the magnetic hysteresis loop is very well known for a FM film coupled with an AFM film where an exchange coupling between the interface spins in AFM and FM gives rise to a shift of the hysteresis loop along the applied magnetic field axis and the magnitude of the shift is defined as the exchange anisotropy field (H_{EB}). This exchange anisotropy is observed when the AFM/FM system is cooled in the presence of a static magnetic field (also known as the cooling field, H_{cool}) to a temperature below T_N . [28,62]. The cooling field aligns all ferromagnetic domains along its direction. The exchange bias phenomenon in the AFM-FM system has been extensively studied for its applications in magnetic read heads, magnetic random access memories, high-density magnetic recording, etc. [63].

MR measurements were performed by the standard van der Pauw method in a PPMS system capable of applying magnetic fields up to 9 T and temperatures down to 2 K. The deposited Fe layer of 8 nm thickness is expected to have in-plane magnetization. As shown in Fig. 6(a), with a magnetic field (as well as the cooling field) applied along the sample surface, the MR measurements show typical anisotropic MR (AMR) during field sweep with two peaks (H_{C1} and H_{C2}) corresponding to the coercive field of the Fe layer [64]. Exchange anisotropy field H_{EB} then can be obtained from the two coercive fields as $H_{EB} = (H_{C1} + H_{C2})/2$. To capture the temperature dependence of the H_{EB} with the in-plane cooling field, we have repeated MR measurements at different temperatures, each time cooling the sample from RT in the presence of the same magnetic field of -2 T along the in-plane direction. Figure 6(a) shows the variation of MR with respect to the magnetic field measured at 2 and 50 K. The MR hysteresis remains symmetric with respect to $B = 0$ at any temperatures from 300 down to 50 K, as shown in Fig. 6(a) for 50 K. Asymmetric MR hysteresis appears below 40 K, due to the exchange bias phenomenon and the relative positions of the peaks are displaced against $B = 0$ into the negative magnetic field direction, as shown in Fig. 6(a) at 2 K. MR hysteresis measured on a controlled sample without the Cr_2Se_3 layer [Fig. S3(b) in Ref. [25]] remained symmetric for all temperatures (as shown in Fig. S4 in Ref. [25]), confirming that the shift observed in the Cr_2Se_3 layer coupled with the Fe film is due to an exchange bias from the Cr_2Se_3 layer. The obtained exchange bias fields (H_{EB}) at different temperatures, for a cooling field, $H_{cool} = -2$ T, are plotted (blue curve) in Fig. 6(b). The curve shows a detectable nonzero H_{EB} at and below 40 K. The temperature above which the exchange bias vanishes is the blocking temperature (T_B). It has been reported that thin AFM films with smaller grain sizes often show a lower blocking temperature than the bulk sample Néel temperatures ($T_B < T_N$) [28,65,66]. Equal blocking and Néel temperatures ($T_B \approx T_N$) are observed when the thickness of the AFM layer is increased [28,66–69]. In our case, the exchange bias effect yields the blocking temperature ($T_B \sim 40$ K) which is quite close to the reported T_N values of bulk Cr_2Se_3 samples ($T_N \sim 42$ – 45 K) [6–9]. As the temperature is lowered below 40 K, the exchange coupling increases the shift in the peaks and hence, increasing H_{EB} [blue curve in Fig. 6(b)]. With lower temperature, the net magnetization of the AFM layer along the interface induced by the exchange interaction during field

cooling also increases [70–74]. The corresponding coercive field defined as $[H_C = |H_{C1} - H_{C2}|/2]$ also increases with decreasing temperature, as shown in Fig. 6(b) (red curve). An enhancement in coercivity below T_N is due to the formation of AFM order in the sample. Variation of the two characteristic peaks (H_{C1} and H_{C2}) in AMR measurements with temperature are shown in Fig. S5 in Ref. [25]. Figure 6(c) shows the variation of H_{EB} with temperature for different H_{cool} values. Reversing the direction of H_{cool} also reverses the sign of H_{EB} but the magnitudes remain relatively unchanged. In general, the shift due to the exchange bias is in the direction opposite to the applied cooling field. Hence, with the change in polarity of H_{cool} , corresponding H_{EB} also changes its sign. Corresponding coercivity H_C , shown in the inset, also shows the same trend for different cooling fields (also shown in Fig. S6 in Ref. [25]).

Figure 6(d) shows the variation of H_{EB} with temperature for a cooling field, $H_{cool} = -2$ T, applied along the perpendicular direction to the surface. For comparison, variation of H_{EB} with temperature obtained from in-plane applied fields is also shown in the same figure. It is clearly evident that the magnitude of the exchange bias field is higher along the perpendicular to the surface. Corresponding variation of H_C , and the characteristic peaks (H_{C1} and H_{C2}) are shown in Fig. S7 in Ref. [25]. Previously, both in-plane and out-of-plane exchange bias have been observed in a Co/CoO bilayer film, as well as in different AFM-FM multilayer systems [27,29,75–77]. For the field-cooled samples with the measurement field applied along the easy axis of the FM layer (in-plane), it is expected to have a higher exchange bias. Although the Fe layer is expected to have the easy axis along the surface plane, at all temperatures below 40 K, we observe a higher magnitude of exchange bias for the out-of-plane field orientation. At 2 K, perpendicular H_{EB} is about 3 times higher than that along the surface. This indicates that the exchange bias in our case is highly dependent on the crystalline orientation of the AFM layer that, in turn, may influence the coupling between the AFM and FM layer.

Considering an ideal interface between the AFM and FM layers, an interfacial exchange energy density $\Delta E_{interface}$ of the AFM-FM interface can be estimated as [68]

$$\Delta E_{interface} = |H_{EB}| M_{S(FM)} t_{FM}, \quad (2)$$

where $|H_{EB}|$ is the magnitude of exchange bias; $M_{S(FM)}$ and t_{FM} are the saturation magnetization and the thickness of the FM layer, respectively. Figure S8 shows the variation of $\Delta E_{interface}$ at different temperatures for the magnetic field applied along the surface [25]. Considering the FM layer thickness (t_{FM}) of 8 nm and $M_{S(FM)} \sim 1420$ emu/cm³, and $|H_{EB}| \sim 292$ Oe at 2 K obtained with in-plane magnetic fields, we estimate $\Delta E_{interface}$ for the Cr_2Se_3/Fe interface is ~ 0.3 erg/cm². For the magnetic field applied perpendicular to the surface, $\Delta E_{interface}$ at 2 K is ~ 1 erg/cm² (as shown in Fig. S9 in Ref. [25]), which is about 3 times higher than that along the plane. The difference in the values of interface energy densities for the two directions perpendicular to each other could arise from the preferential orientation of the spins due to crystallinity of the layers [78].

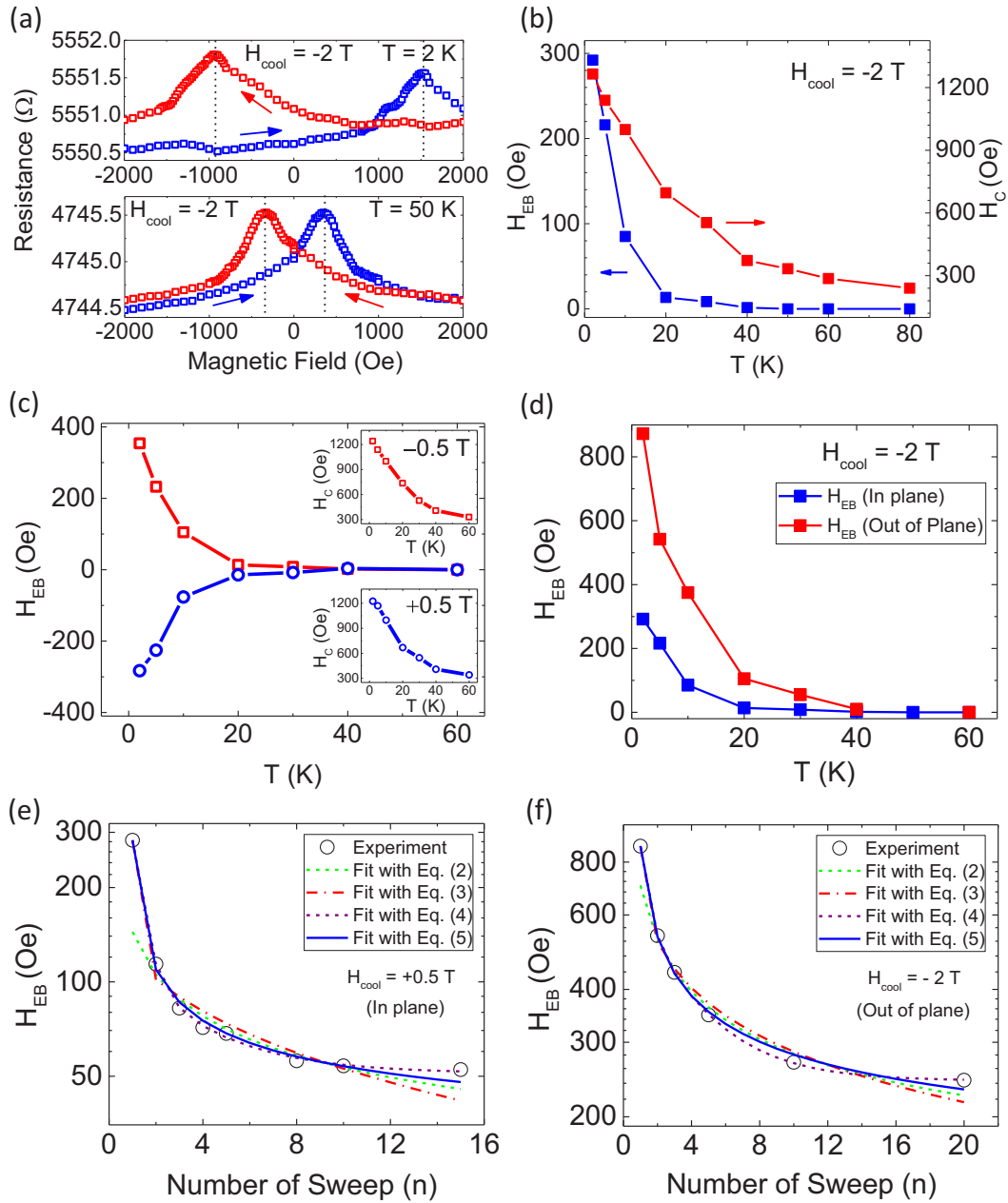


FIG. 6. Magnetoresistance measurement results of a 25-nm Cr_2Se_3 film grown on $\text{Si}(111)-7 \times 7$ surfaces. (a) In-plane magnetic field dependence of the longitudinal magnetoresistance of $\text{Ta}/\text{Fe}/\text{Cr}_2\text{Se}_3/\text{Si}(111)$ at 2 and 50 K. Vertical dotted lines represent the characteristic values H_{C1} (decreasing field) and H_{C2} (increasing field), for cooling field $H_{\text{cool}} = -2$ T. (b) Temperature dependence of in-plane exchange bias field (H_{EB}) and coercive field (H_C). (c) Temperature dependence of H_{EB} for different cooling fields. Corresponding coercive fields are also shown (inset). (d) Temperature dependence of out-of-plane H_{EB} . The in-plane H_{EB} is also plotted for comparison. The cooling field is -2 T for both measurements. (e) Variation of H_{EB} with number of field cycles (n) after in-plane field cooling demonstrating the training effect for the applied field along the surface. The open circles and the lines represent the experimental data points and fit to the experimental data using different models, respectively. (f) Variation of the training for the out-of-plane H_{EB} with number of field cycles (n). Experimental data (open circles) are fitted with different models (lines).

D. Exchange bias training effect

Both H_{EB} and H_C tend to decrease monotonically when the AMR measurement is repeated multiple times at the same temperature after the initial field cooling, which is known as the training effect [31]. Absence of a net magnetic moment in an AFM produces no net Zeeman energy in an external magnetic field, which results in randomly oriented domains

during the first field cooling from above the Néel temperature. Multiple cycling of the hysteresis loop gradually rearranges the spin structure of the AFM layer relaxing it towards its ground state giving the observed training effect [35,79]. The strength of the training effect depends mostly on the exchange interaction at the interface, the change of the nonequilibrium spin moment of the AFM domains, and on the thermal energy. Figure 6(e) shows the dependence of in-plane H_{EB} on the

loop number (n) measured for 15 consecutive cycles at 2 K after initial field cooling with $H_{\text{cool}} = 0.5$ T. Corresponding in-plane H_C , in Fig. S10, also shows a decreasing trend with the number of sweeps [25]. The drop in H_{EB} is maximum only after the first cycle (down to $\sim 40\%$), as shown in the inset in Fig. S10 in Ref. [25]. The variation is less for the subsequent cycles ($\sim 20\%$, only) and stabilizes towards a constant level, all of which point towards some underlying relaxation dynamics at the AFM-FM interface. Although the microscopic origin is still debatable, different theoretical models were proposed to explain the training effect of H_{EB} based on the time dependence of the interface spin moment of the AFM layer. We attempt to analyze the observed training effect by fitting our experimental data with different models.

We first follow the thermal relaxation model, where the dependence of H_{EB} and the number of cycles (n) follows a simple empirical power law [31]:

$$H_{\text{EB}}(n) = H_{\text{EB}}(\infty) + \frac{k_H}{\sqrt{n}}, \quad (3)$$

where $H_{\text{EB}}(n)$ and $H_{\text{EB}}(\infty)$ are the exchange bias fields at the n th cycle, and in the limit of infinite cycles ($n \rightarrow \infty$), respectively, and k_H is a system-dependent constant. The fit result with Eq. (3), as shown in Fig. 6(e) (green dashed line), is in good agreement with experimental data for $n > 1$, which is consistent with previous studies in the literature [35,68]. The fit breaks down and results in a negative $H_{\text{EB}}(\infty)$ if the data point at $n = 1$ is included. Excluding the data at $n = 1$, the values of $H_{\text{EB}}(\infty)$ and k_H obtained are 11.2 and 133.2 Oe, respectively. To explain the variation of H_{EB} including $n = 1$, Binek [35] derived the following relation for the exchange bias training effect:

$$H_{\text{EB}}(n+1) = H_{\text{EB}}(n) + \gamma_H [H_{\text{EB}}(n) - H_{\text{EB}}(\infty)]^3, \quad (4)$$

where γ_H is a system-dependent constant. Eq. (3) recovers the empirical power law, Eq. (2), in the limit of $n \gg 1$ with $2\gamma_H = 1/k_H^2$ [35]. However, the fit using Eq. (3) including $n = 1$ data is not satisfactory in our case either, unless a negative $H_{\text{EB}}(\infty)$ is allowed [red dashed line in Fig. 6(e)]. Excluding the $n = 1$ data point allows a better fit to the data (shown in Fig. S11 in Ref. [25]) giving $H_{\text{EB}}(\infty) = 23.8$ Oe and γ_H about 445.6×10^{-7} Oe $^{-2}$ corresponding to $k_H = 105.9$ Oe.

To allow for a positive $H_{\text{EB}}(\infty)$ and explain the change of H_{EB} including the $n = 1$ data, we consider an alternative model [46,47] that describes the training effect using exponential time dependence of a mixed state of frozen and rotatable uncompensated spins at the interface:

$$H_{\text{EB}}(n) = H_{\text{EB}}(\infty) + A_f \exp\left(-\frac{n}{P_f}\right) + A_i \exp\left(-\frac{n}{P_i}\right), \quad (5)$$

where A_f and P_f are parameters related to the changes of the frozen spins and A_i and P_i are parameters for the rotatable spin component at the AFM-FM interface. Here, dimensionless parameters P_f and P_i act as the relaxation time constants for the exponential decay of the spin components towards equilibrium. The above equation fits the experimental data very well [purple dashed line in Fig. 6(e)] indicating a complex spin arrangement at the interface. The parameter values

obtained from the fit are $H_{\text{EB}}(\infty) = 51.2$ Oe, $A_f = 71.9$ Oe, $P_f = 3.2$, $A_i = 1333.2$, and $P_i = 0.5$. The associated larger prefactor $A_i \gg A_f$ and the relaxation time ratio $P_f/P_i \sim 6.48$ indicate that the exchange bias is governed mainly by the interface spins. However, this model predicts a much higher $H_{\text{EB}}(\infty) = 51.2$ Oe, compared to Eqs. (3) and (4) (excluding $n = 1$ data).

To explain our data with the same physical model of Binek [35] and to allow for a positive $H_{\text{EB}}(\infty)$ including the $n = 1$ data, we next consider a modified power-law model [38,39],

$$H_{\text{EB}}(n) = H_{\text{EB}}(\infty) + k_H [n + n_0]^{-0.5}, \quad (6)$$

where k_H is the same constant as in Eq. (3), and n_0 is a dimensionless number. It should be noted that both Eqs. (3) and (4) can be derived from Eq. (6) under certain approximations (see Sec. S12 in the Supplemental Material [25]). H_{EB} obtained from Eq. (6) allows a much better fit to our experimental data [blue solid line in Fig. 6(e)] including the $n = 1$ data point compared to Eq. (3) or (4), while preserving the power-law dependence. The parameter values obtained from the fit are $H_{\text{EB}}(\infty) = 23.7$ Oe, $k_H = 90.9$ Oe.

The training effect along the out-of-plane direction is shown in Fig. 6(f). Again, a decreasing trend of H_{EB} on the number of sweeps (n) measured for 20 consecutive cycles, at an initial H_{cool} of -2 T and a constant temperature of 2 K, is observed. Corresponding H_C also shows a declining trend with the number of sweeps (as shown in Fig. S13 in Ref. [25]). Fitting the out-of-plane exchange bias training effect for $n > 1$ with Eq. (3) gives $H_{\text{EB}}(\infty) = 86.2$ Oe and $k_H = 618.5$ Oe. Fit using Eq. (4), including $n = 1$, again results in a much lower $H_{\text{EB}}(\infty) = 22.8$ Oe, which improves with the exclusion of the data at $n = 1$ ($H_{\text{EB}}(\infty) = 99.0$ Oe, as shown in Fig. S14 in Ref. [25]). The exponential dependence of Eq. (5) explains the data well including $n = 1$ with parameters obtained as $H_{\text{EB}}(\infty) = 243.4$ Oe, $A_f = 457.6$ Oe, $P_f = 3.4$, $A_i = 2168.1$, and $P_i = 0.5$. Similar to the in-plane case, out-of-plane $H_{\text{EB}}(\infty)$ predicted from Eq. (5) is much higher than that obtained from Eq. (3) or (4) (excluding $n = 1$ data). The relaxation times of frozen and rotatable spins obtained for the out-of-plane training effect are quite close to those obtained from the in-plane training effect. Finally, we fit the data with the power law of Eq. (6) [Fig. 6(f) blue solid line]. The fit could explain the data very well including the $n = 1$ data point, with parameters obtained as $H_{\text{EB}}(\infty) = 120.3$, $k_H = 492.3$ Oe. In the Supplemental Material [25] Secs. S15 and S16, we provide a complete summary of the fitting results of the exchange bias training effect using different models.

The origin of exchange bias is a complex phenomenon that depends on several factors, e.g., interfacial coupling strength, AFM anisotropy, interface domain structure, film thickness, strain, atomic steps, and interface roughness [78]. In addition, exchange bias in epitaxial samples is influenced by the field-cooling direction and intrinsic magnetocrystalline anisotropy of the AFM layer [80–82]. In our case, the AFM layer of Cr_2Se_3 is epitaxially grown along the c axis on a sapphire substrate, whereas the top Fe film is polycrystalline. Hence, the spins in the AFM layer may have a possible magnetic easy axis along the out-of-plane direction [49], and could show enhanced exchange anisotropy when field cooled with a magnetic field applied perpendicular to the surface. In

addition, depending on the directions, the magnetic field interacts differently with the uncompensated spins (which cannot be ruled out) along with the compensated, and can produce a complex picture in the experiment. A bilayer of a Cr_2Se_3 layer coupled with another (001)-oriented ferromagnetic thin film with a hexagonal crystal structure and a perpendicular magnetic anisotropy (e.g., Cr_2Te_3 thin film, Ref. [49]) would be an interesting out-of-plane exchange bias system to study. However, to obtain a deeper understanding of the exchange bias and the training effect in epitaxial Cr_2Se_3 thin films of different thicknesses, further theoretical and experimental studies on its time dependence as well as the spin structure of the AFM-FM system close to the interface should be done in detail.

IV. SUMMARY AND CONCLUSION

In conclusion, we have carried out the MBE growth of Cr_2Se_3 thin films on insulating $c\text{-Al}_2\text{O}_3(0001)$ and $\text{Si}(111)\text{-}(7 \times 7)$ substrates. Structural, electrical, and magnetic properties of the films have been characterized by several *in situ* and *ex situ* techniques. Sharp streaks in RHEED patterns imply smooth thin-film growth on both substrates. The film has hexagonal structure and is oriented along the (001) direction

(c axis), as confirmed from *in situ* RHEED and STM, and *ex situ* XRD. Chemical composition of the film is investigated through *in situ* XPS measurement. Electrical measurement on the as-grown film shows a narrow band gap semiconducting behavior. The antiferromagnetic nature of the grown film is confirmed from the magnetotransport measurements of an exchange coupled system of $\text{Cr}_2\text{Se}_3(\text{AFM})\text{-Fe}(\text{FM})$. Exchange bias is higher in magnitude along the out-of-plane direction compared to that in the in-plane direction. The exchange bias training effect in both directions seems to be consistent with a modified power-law decay behavior. Our results indicate that epitaxial Cr_2Se_3 thin films could offer an interesting materials system to study effects of magnetic anisotropy and field-cooling direction on the exchange bias properties in fully epitaxial AFM-FM bilayers.

ACKNOWLEDGMENTS

This work was supported in part by an NSF EFRI grant, NSF NASCENT ERC, and NSF NNCI (done at the Texas Nanofabrication Facility at the University of Texas at Austin supported by NSF Grant No. NNCI-1542159). We appreciate technical support from Omicron.

The authors declare no competing financial interest.

-
- [1] J. Wontcheu, W. Bensch, S. Mankovsky, S. Polesya, and H. Ebert, Effect of anion substitution onto structural and magnetic properties of chromium chalcogenides, *Prog. Solid State Chem.* **37**, 226 (2009).
- [2] A. Kjekshus and W. B. Pearson, Phases with the nickel arsenide and closely-related structures, *Prog. Solid State Chem.* **1**, 83 (1964).
- [3] M. Chevreton, M. Murat, C. Eyraud, and E. F. Bertaut, Structure et conductibilité électrique des composés à lacunes ordonnées du système chrome-sélénium, *J. Phys. (Paris)* **24**, 443 (1963).
- [4] F. H. Wehmeier, E. T. Keve, and S. C. Abrahams, Preparation, structure, and properties of some chromium selenides. Crystal growth with selenium vapor as a novel transport agent, *Inorg. Chem.* **9**, 2125 (1970).
- [5] S. Ohta, Y. Adachi, T. Kaneko, M. Yuzuri, and H. Yoshida, Thermal expansion in chromium chalcogenides Cr_2X_3 ($\text{X}=\text{Se}, \text{Te}$), *J. Phys. Soc. Jpn.* **63**, 2225 (1994).
- [6] Y. Adachi, M. Yuzuri, T. Kaneko, S. Abe, and H. Yoshida, Magnetic phase transition of Cr_2Se_3 , *J. Phys. Soc. Jpn.* **63**, 369 (1994).
- [7] Y. Adachi, M. Ohashi, T. Kaneko, M. Yuzuri, Y. Yamaguchi, S. Funahashi, and Y. Morii, Magnetic structure of rhombohedral Cr_2Se_3 , *J. Phys. Soc. Jpn.* **63**, 1548 (1994).
- [8] M. Yuzuri, Magnetic properties of the compound Cr-Se System, *J. Phys. Soc. Jpn.* **35**, 1252 (1973).
- [9] S. Ohta, Y. Narui, and Y. Sakayori, Effect of Te-substitution on magnetic properties of $\text{Cr}_2\text{Se}_{3-y}\text{Te}_y$ ($0 \leq y \leq 0.15$), *J. Magn. Mater.* **170**, 168 (1997).
- [10] T. Zhang, X. Su, Y. Yan, W. Liu, T. Hu, C. Zhang, Z. Zhang, and X. Tang, Enhanced thermoelectric properties of codoped Cr_2Se_3 : The distinct roles of transition metals and S, *ACS Appl. Mater. Interfaces* **10**, 22389 (2018).
- [11] T. Zhang, X. Su, Y. Yan, W. Liu, Y. You, H. Xie, D. Yang, C. Uher, and X. Tang, Structure and thermoelectric properties of 2D $\text{Cr}_2\text{Se}_{3-3x}\text{S}_{3x}$ solid solutions, *J. Mater. Chem. C* **6**, 836 (2018).
- [12] T. Zhang, X. Su, J. Li, Z. Li, Y. Yan, W. Liu, and X. Tang, Structure and improved thermoelectric properties of $\text{Ag}_{2x}\text{Cr}_{2-2x}\text{Se}_3$ compounds, *Inorg. Chem.* **57**, 12125 (2018).
- [13] Q. Guo, D. Berthebaud, J. Ueda, S. Tanabe, A. Miyoshi, K. Maeda, and T. Mori, Facile p-n control, and magnetic and thermoelectric properties of chromium selenides $\text{Cr}_{2+x}\text{Se}_3$, *J. Mater. Chem. C* **7**, 8269 (2019).
- [14] K. R. Pisharody, Thermoelectric properties of chromium sulfoselenides, *J. Solid State Chem.* **30**, 149 (1979).
- [15] S. Ramaraj, S. Mani, S.-M. Chen, S. Palanisamy, V. Velusamy, J. M. Hall, T.-W. Chen, and T.-W. Tseng, Hydrothermal synthesis of Cr_2Se_3 hexagons for sensitive and low-level detection of 4-nitrophenol in water, *Sci. Rep.* **8**, 4839 (2018).
- [16] R. Blachnik, P. G. Gunia, M. Fischer, and H. D. Lutz, Das system chrom-selen, *J. Less Common Met.* **134**, 169 (1987).
- [17] M. Deng, V. Hrkac, U. Schurmann, B. Erkartal, N. Wolff, K. Gerwien, B. Hesseler, F. Beiroth, W. Bensch, V. Duppel, and L. Kienle, Nanocomposite $\text{CdSe}/\text{Cr}_2\text{Se}_3$: Synthesis, Characterization, and in situ Transformation Study, *Z. Anorg. Allg. Chem.* **641**, 214 (2015).
- [18] A. Sobhani and M. Salavati-Niasari, Chromium selenide nanoparticles: Hydrothermal synthesis in the presence of a new selenium source, *J. Nanostruct.* **7**, 141 (2017).
- [19] K. Sato, Y. Aman, M. Hirai, and M. Fujisawa, Reflectivity spectra in single crystals of Cr_3Te_4 , Cr_2Te_3 and Cr_2Se_3 between 0.3 and 23 eV, *J. Phys. Soc. Jpn.* **59**, 435 (1990).
- [20] J. Yan, X. Luo, F. C. Chen, Q. L. Pei, G. T. Lin, Y. Y. Han, L. Hu, P. Tong, W. H. Song, X. B. Zhu, and Y. P. Sun, Anomalous

- Hall effect in two-dimensional non-collinear antiferromagnetic semiconductor $\text{Cr}_{0.68}\text{Se}$, *Appl. Phys. Lett.* **111**, 022401 (2017).
- [21] C.-H. Ho and X.-R. Lai, Effect of Cr on the structure and property of $\text{Mo}_{1-x}\text{Cr}_x\text{Se}_2$ ($0 \leq x \leq 0.2$) and Cr_2Se_3 , *ACS Appl. Electron. Mater.* **1**, 370 (2019).
- [22] S. Ohta, Y. Narui, and M. Ohwatari, Electrical properties of $\text{Cr}_{1-\delta}\text{Se}$ ($0.07 \leq \delta \leq 0.33$), *J. Phys. Soc. Jpn.* **65**, 3084 (1996).
- [23] A. Roy, S. Guchhait, S. Sonde, R. Dey, T. Pramanik, A. Rai, H. C. P. Movva, L. Colombo, and S. K. Banerjee, Two-dimensional weak anti-localization in Bi_2Te_3 thin film grown on $\text{Si}(111)$ - (7×7) surface by molecular beam epitaxy, *Appl. Phys. Lett.* **102**, 163118 (2013).
- [24] A. Roy, K. Bhattacharjee, and B. N. Dev, Growth of $(\sqrt{3} \times \sqrt{3})$ -Ag and (111) oriented Ag islands on $\text{Ge}/\text{Si}(111)$ surfaces, *Appl. Surf. Sci.* **256**, 508 (2009).
- [25] See Supplemental Material at <http://link.aps.org/supplemental/10.1103/PhysRevMaterials.4.025001> for additional details regarding the growth of Cr_2Se_3 of different thicknesses, band gap, exchange bias, and modeling of the in-plane and out-of-plane training effect (Secs. S1-S16). S1: RHEED from Cr_2Se_3 thin films of different thicknesses. S2: Estimation of band gap assuming temperature-dependent mobility. S3: Schematic of exchange bias system and controlled sample. S4: Exchange bias in a controlled sample. S5: Temperature dependence of characteristic peaks (H_{C1} and H_{C2}) with in-plane field. S6: Temperature dependence of exchange bias and coercive field for varying cooling fields. S7: Temperature dependence of characteristic peaks (H_{C1} and H_{C2}) with out-of-plane field. S8: Temperature variation of in-plane interface energy per unit area. S9: Temperature variation of out-of-plane interface energy per unit area. S10: In-plane training effect. S11: Fit to the in-plane training effect using Eq. (4) excluding $n = 1$. S12: Derivation of the modified power-law equation [Eq. (6)]. S13: Out-of-plane training effect. S14: Fit to the out-of-plane training effect using Eq. (4) excluding $n = 1$. S15: Parameters obtained from the fit to the exchange bias training effect. S16: Validity of training effect fit with Eq. (4).
- [26] Y. J. Chen, D. K. Lottis, E. D. Dahlberg, J. N. Kuznia, A. M. Wowchak, and P. I. Cohen, Exchange effects in molecular-beam-epitaxy grown iron films, *J. Appl. Phys.* **69**, 4523 (1991).
- [27] M. P. Proenca, J. Ventura, C. T. Sousa, M. Vazquez, and J. P. Araujo, Exchange bias, training effect, and bimodal distribution of blocking temperatures in electrodeposited core-shell nanotubes, *Phys. Rev. B* **87**, 134404 (2013).
- [28] J. Noguez and I. K. Schuller, Exchange bias, *J. Magn. Magn. Mater.* **192**, 203 (1999).
- [29] S. Maat, K. Takano, S. S. P. Parkin, and E. E. Fullerton, Perpendicular Exchange Bias of Co/Pt Multilayers, *Phys. Rev. Lett.* **87**, 087202 (2001).
- [30] J. Ventura, J. P. Araujo, J. B. Sousa, A. Veloso, and P. P. Freitas, Training effect in specular spin valves, *Phys. Rev. B* **77**, 184404 (2008).
- [31] D. Paccard, C. Schlenker, O. Massenet, R. Montmory, and A. Yelon, A new property of ferromagnetic-antiferromagnetic coupling, *Phys. Status Solidi B* **16**, 301 (1966).
- [32] L. E. Fernandez-Outon, G. Vallejo-Fernandez, S. Manzoor, and K. O'Grady, Thermal instabilities in exchange biased materials, *J. Magn. Magn. Mater.* **303**, 296 (2006).
- [33] P. V. Muhammed Shameem and M. Senthil Kumar, Training effect of the exchange bias in sputter deposited Fe_3O_4 thin films with varying thickness, *J. Magn. Magn. Mater.* **458**, 241 (2018).
- [34] A. Hoffmann, Symmetry Driven Irreversibilities at Ferromagnetic-Antiferromagnetic Interfaces, *Phys. Rev. Lett.* **93**, 097203 (2004).
- [35] C. Binek, Training of the exchange-bias effect: A simple analytic approach, *Phys. Rev. B* **70**, 014421 (2004).
- [36] L. D. Landau and I. T. Khalatnikov, On the anomalous absorption of sound near a second order phase transition point, *Dokl. Akad. Nauk SSSR* **96**, 469 (1954).
- [37] G. Vizdrik, S. Ducharme, V. M. Fridkin, and S. G. Yudin, Kinetics of ferroelectric switching in ultrathin films, *Phys. Rev. B* **68**, 094113 (2003).
- [38] W. B. Rui, M. C. He, B. You, Z. Shi, S. M. Zhou, M. W. Xiao, Y. Gao, W. Zhang, L. Sun, and J. Du, Asymmetric exchange bias training effect in spin glass (FeAu)/ FeNi bilayers, *Chin. Phys. B* **23**, 107502 (2014).
- [39] Y. Su and J. Hu, Exchange bias training effect under different energy dissipation pattern, *J. Appl. Phys.* **112**, 043906 (2012).
- [40] Q. Xu, Z. Xu, M. He, Y. Cao, and J. Du, Irreversible electrical manipulation of magnetization on BiFeO_3 -based heterostructures, *J. Appl. Phys.* **117**, 17D707 (2015).
- [41] M. C. He, B. You, H. Q. Tu, Y. Sheng, Q. Y. Xu, W. B. Rui, Y. Gao, Y. Q. Zhang, Y. B. Xu, and J. Du, Temperature dependent exchange bias training effect in single-crystalline BiFeO_3/Co bilayers, *J. Appl. Phys.* **117**, 17C745 (2015).
- [42] B. B. Singh and S. Chaudhary, Study of angular dependence of exchange bias and misalignment in uniaxial and unidirectional anisotropy in $\text{NiFe}(111)/\text{FeMn}(111)/\text{CoFeB}$ (amorphous) stack, *J. Magn. Magn. Mater.* **385**, 166 (2015).
- [43] X. Xue, X. Yuan, W. Rui, Q. Xu, B. You, W. Zhang, S. Zhou, and J. Du, Temperature dependent exchange bias effect in polycrystalline BiFeO_3/FM ($\text{FM} = \text{NiFe}, \text{Co}$) bilayers, *Eur. Phys. J. B* **86**, 121 (2013).
- [44] Y. Zhang, W. Rui, Z. Shi, S. Zhou, M. Yang, B. You, and J. Du, A simple model to describe different types of exchange bias training effect, *J. Supercond. Novel Magn.* **29**, 531 (2016).
- [45] C. Zhang, S. Y. Wang, W. F. Liu, X. L. Xu, X. Li, H. Zhang, J. Gao, and D. J. Li, Room temperature exchange bias in multi-ferroic BiFeO_3 nano- and microcrystals with antiferromagnetic core and two-dimensional diluted antiferromagnetic shell, *J. Nanopart. Res.* **19**, 182 (2017).
- [46] F. Radu and H. Zabel, Exchange bias effect of ferro-/antiferromagnetic heterostructures, in *Magnetic Heterostructures*, Springer Tracts in Modern Physics Vol. 227, edited by H. Zabel and S. D. Bader (Springer, Berlin, Heidelberg, 2008), pp. 97–184.
- [47] S. K. Mishra, F. Radu, H. A. Dürr, and W. Eberhardt, Training-Induced Positive Exchange Bias in NiFe/IrMn Bilayers, *Phys. Rev. Lett.* **102**, 177208 (2009).
- [48] S. Sahoo, S. Polisetty, and Ch. Binek, Dynamic enhancement of the exchange bias training effect, *J. Appl. Phys.* **101**, 053902 (2007).
- [49] A. Roy, S. Guchhait, R. Dey, T. Pramanik, C.-C. Hsieh, A. Rai, and S. K. Banerjee, Perpendicular magnetic anisotropy and spin glass-like behavior in molecular beam epitaxy grown chromium telluride thin films, *ACS Nano* **9**, 3772 (2015).
- [50] R. Dey, A. Roy, T. Pramanik, S. Guchhait, S. Sonde, A. Rai, L. F. Register, and S. K. Banerjee, Localization and interaction

- effects of epitaxial Bi₂Se₃ bulk states in two-dimensional limit, *J. Appl. Phys.* **120**, 164301 (2016).
- [51] J. Park, Y.-A. Soh, G. Aeppli, S. R. Bland, X.-G. Zhu, X. Chen, Q.-K. Xue, and F. Grey, Crystal structure and epitaxy of Bi₂Te₃ films grown on Si, *Appl. Phys. Lett.* **101**, 221910 (2012).
- [52] T. Michely, M. Hohage, M. Bott, and G. Comsa, Inversion of Growth Speed Anisotropy in Two Dimensions, *Phys. Rev. Lett.* **70**, 3943 (1993).
- [53] S. Liu, Z. Zhang, G. Comsa, and H. Metiu, Kinetic Mechanism for Island Shape Variations Caused by Changes in the Growth Temperature, *Phys. Rev. Lett.* **71**, 2967 (1993).
- [54] M. C. Biesinger, L. W. M. Lau, A. R. Gerson, and R. St. C. Smart, Resolving surface chemical states in XPS analysis of first row transition metals, oxides and hydroxides: Sc, Ti, V, Cu and Zn, *Appl. Surf. Sci.* **257**, 887 (2010).
- [55] D. Briggs, XPS: Basic principles, spectral features and qualitative analysis, in *Surface Analysis by Auger and X-Ray Photoelectron Spectroscopy*, edited by D. Briggs and J. T. Grant (IM Publications, Chichester, UK, 2003), pp. 31–56.
- [56] E. Agostinelli, C. Battistoni, D. Fiorani, G. Mattogno, and M. Nogues, An XPS study of the electronic structure of the Zn_xCd_{1-x}Cr₂(X = S, Se) spinel system, *J. Phys. Chem. Solids* **50**, 269 (1989).
- [57] V. A. Ivanova, D. S. Abdinov, and G. M. Alien, On Some Characteristics of Chromium Selenides, *Phys. Status Solidi* **24**, K145 (1967).
- [58] D. Babot and M. Chevreton, Conductibilité électrique aux basses températures des composés binaires Cr₂X₃ et Cr₃X₄ (X = S, Se ou Te), *J. Solid State Chem.* **8**, 166 (1973).
- [59] J. B. Goodenough, A. Hamnett, G. Huber, F. Hullinger, M. Leib, S. K. Ramasesha, and H. Werheit, in *Physics of Non-Tetrahedrally Bonded Binary Compounds III*, edited by O. Madelung (Springer-Verlag, Berlin, Heidelberg, 1984), Chap. 9.15.3.
- [60] S. M. Sze and K. K. Ng, *Physics of Semiconductor Devices*, 3rd ed. (John Wiley & Sons, Inc., New York, 2007).
- [61] Y. A. Freiman and H. J. Jodl, Solid oxygen, *Phys. Rep.* **401**, 1 (2004).
- [62] W. H. Meiklejohn and C. P. Bean, New magnetic anisotropy, *Phys. Rev.* **102**, 1413 (1956).
- [63] C. Chappert, A. Fert, and F. N. Van Dau, The emergence of spin electronics in data storage, *Nat. Mater.* **6**, 813 (2007).
- [64] D. A. Gilbert, B. B. Maranville, A. L. Balk, B. J. Kirby, P. Fischer, D. T. Piercen, J. Unguris, J. A. Borchers, and K. Liu, Realization of ground-state artificial skyrmion lattices at room temperature, *Nat. Commun.* **6**, 8462 (2015).
- [65] S. Soeya, H. Hoshiya, M. Fuyama, and S. Tadokoro, Exchange coupling between ferromagnetic fcc Ni₈₁Fe₁₉ and antiferromagnetic bcc CrMnPt films, *J. Appl. Phys.* **80**, 1006 (1996).
- [66] S. N. K. Hoshino, R. Nakatani, H. Hoshiya, and Y. Sugita, Magnetoresistance and interlayer exchange coupling between magnetic layers in Fe–Mn/Ni–Fe–Co/Cu/Ni–Fe–Co Multilayers, *Jpn. J. Appl. Phys.* **33**, 1327 (1994).
- [67] T. J. Moran, J. M. Gallego, and I. K. Schuller, Increased exchange anisotropy due to disorder at permalloy/CoO interfaces, *J. Appl. Phys.* **78**, 1887 (1995).
- [68] J. Nogues, D. Lederman, T. J. Moran, I. K. Schuller, and K. V. Rao, Large exchange bias and its connection to interface structure in FeF₂–Fe bilayers, *Appl. Phys. Lett.* **68**, 3186 (1996).
- [69] G. Choe and S. Gupta, High exchange anisotropy and high blocking temperature in strongly textured NiFe(111)/FeMn(111) films, *Appl. Phys. Lett.* **70**, 1766 (1997).
- [70] J. Keller, P. Miltényi, B. Beschoten, G. Güntherodt, U. Nowak, and K. D. Usadel, Domain state model for exchange bias. II. Experiments, *Phys. Rev. B* **66**, 014431 (2002).
- [71] M. Fecioru-Morariu, S. R. Ali, C. Papusoi, M. Sperlich, and G. Güntherodt, Effects of Cu Dilution in IrMn on the Exchange Bias of CoFe / IrMn Bilayers, *Phys. Rev. Lett.* **99**, 097206 (2007).
- [72] L. C. Sampaio, A. Mougin, J. Ferré, P. Georges, A. Brun, H. Bernas, S. Poppe, T. Mewes, J. Fassbender, and B. Hillebrands, Probing interface magnetism in the FeMn/NiFe exchange bias system using magnetic second-harmonic generation, *Europhys. Lett.* **63**, 819 (2003).
- [73] R. Morales, Z. P. Li, J. Olamit, K. Liu, J. M. Alameda, and I. K. Schuller, Role of the Antiferromagnetic Bulk Spin Structure on Exchange Bias, *Phys. Rev. Lett.* **102**, 097201 (2009).
- [74] Y. Shiratsuchi, H. Noutomi, H. Oikawa, T. Nakamura, M. Suzuki, T. Fujita, K. Arakawa, Y. Takechi, H. Mori, T. Kinoshita, M. Yamamoto, and R. Nakatani, Detection and *In Situ* Switching of Unreversed Interfacial Antiferromagnetic Spins in a Perpendicular-Exchange-Biased System, *Phys. Rev. Lett.* **109**, 077202 (2012).
- [75] E. Shipton, K. Chan, T. Hauet, O. Hellwig, and E. E. Fullerton, Suppression of the perpendicular anisotropy at the CoO Néel temperature in exchange-biased CoO/[Co/Pt] multilayers, *Appl. Phys. Lett.* **95**, 132509 (2009).
- [76] L. Sun, S. M. Zhou, P. C. Searson, and C. L. Chien, Longitudinal and perpendicular exchange bias in FeMn/(FeNi/FeMn)_n Multilayers, *J. Appl. Phys.* **93**, 6841 (2003).
- [77] N. N. Phuoc and T. Suzuki, In-Plane and Out-of-Plane Exchange Biases in Epitaxial FePt–FeMn Multilayers with Different Crystalline Orientations, *IEEE Trans. Magn.* **44**, 2828 (2008).
- [78] N. H. Dung, N. P. Thuy, N. A. Tuan, and N. N. Phuoc, Out-of-plane exchange bias and magnetic anisotropy in MnPd/Co multilayers, *J. Magn. Magn. Mater.* **320**, 3334 (2008).
- [79] Ch. Binek, X. He, and S. Polisetty, Temperature dependence of the training effect in a Co/CoO exchange-bias layer, *Phys. Rev. B* **72**, 054408 (2005).
- [80] M. T. Hutchings, B. D. Rainford, and H. J. Guggenheim, Spin waves in antiferromagnetic FeF₂, *J. Phys. C* **3**, 307 (1970).
- [81] H. Shi and D. Lederman, Exchange bias flop in Fe_xZn_{1-x}F₂/Co bilayers, *Phys. Rev. B* **66**, 094426 (2002).
- [82] W. Zhang and K. M. Krishnan, Epitaxial exchange-bias systems: From fundamentals to future spin-orbitronics, *Mater. Sci. Eng., R* **105**, 1 (2016).